ADVANCES IN ATMOSPHERIC SCIENCES, VOL. 41, SEPTEMBER 2024, 1721–1734

• **Original Paper** •

Microphysical Characteristics of Rainfall Based on Long-Term Observations with a 2DVD in Yangbajain, Tibet

Ming LI[1,2], Yongheng BI[*2,3], Yonghai SHEN[2,3], Yinan WANG[2,3], Ciren Nima[1], Tianlu CHEN[1], and Daren LYU[*2,3]

[1]*Key Laboratory for Cosmic Rays of the Ministry of Education*, *Tibet University*, *Lhasa* 850000, *China*

[2]*Key Laboratory of Middle Atmosphere and Global Environment Observation (LAGEO)*, *Institute of Atmospheric Physics*, *Chinese Academy of Science*, *Beijing* 100029, *China*

[3]*University of Chinese Academy of Sciences*, *Beijing* 100049, *China*

(Received 29 October 2023; revised 18 January 2024; accepted 23 January 2024)

ABSTRACT

Raindrop size distribution (DSD) plays a crucial role in enhancing the accuracy of radar quantitative precipitation estimates in the Tibetan Plateau (TP). However, there is a notable scarcity of long-term, high-resolution observations in this region. To address this issue, long-term observations from a two-dimensional video disdrometer (2DVD) were leveraged to refine the radar and satellite-based algorithms for quantifying precipitation in the hinterland of the TP. It was observed that weak precipitation (R<1, mm h^{-1}) accounts for 86% of the total precipitation time, while small raindrops (D<2 mm) comprise 99% of the total raindrop count. Furthermore, the average spectral width of the DSD increases with increasing rain rate. The DSD characteristics of convective and stratiform precipitation were discussed across five different rain rates, revealing that convective precipitation in Yangbajain (YBJ) exhibits characteristics similar to maritime-like precipitation. The constrained relationships between the slope Λ and shape μ, D_m and N_w of gamma DSDs were derived. Additionally, we established a correlation between the equivalent diameter and drop axis ratio and found that raindrops on the TP attain a nearly spherical shape. Consequently, the application of the rainfall retrieval algorithms of the dual-frequency precipitation radar in the TP is improved based on the statistical results of the DSD.

Key words: Tibetan Plateau, raindrop size distribution, 2DVD, dual frequency radar, microphysical features

Citation: Li, M., Y. H. Bi, Y. H. Shen, Y. N. Wang, C. R. Nima, T. L. Chen, and D. R. Lyu, 2024: Microphysical characteristics of rainfall based on long-term observations with a 2DVD in Yangbajain, Tibet. *Adv. Atmos. Sci.*, **41**(9), 1721–1734, https://doi.org/10.1007/s00376-024-3299-3.

Article Highlights:

- In YBJ, weak precipitation accounted for 86% of the total precipitation time, while small raindrops comprised 99% of the total raindrop count.
- While stratiform precipitation dominates in the TP hinterland, convective precipitation also contributes significantly to short-term rainfall.
- The modified dual-frequency ratio method in the TP hinterland avoids the dual-value phenomenon in the dual-frequency precipitation radar rainfall retrieval algorithm.

1. Introduction

The Tibetan Plateau (TP), recognized as the "third pole" of the Earth, is situated in southwestern China with an average elevation of over 4000 m. Its distinctive high altitude, surface features, and climate profoundly influence the climate and water cycle not only in China and Asia but also globally, earning it the title "Water Tower of Asia" (Chen et al., 2017). The water vapor on the TP mainly comes from the Indian Ocean monsoon and the westerly wind belt, in addition to its own water cycle (Yuan et al., 2023). The precipitation on the TP significantly impacts the water cycle of the plateau itself and the middle and lower reaches of the Yangtze River. Due to the harsh environment and limited observation data available on the TP, research is lacking on the precipitation characteristics in this region. However, due to the special nature and importance of the TP, we need to carry out long-term observations of precipitation on the TP to obtain long-term, accurate, and representative results.

* Corresponding authors: Yongheng BI, Daren LYU
Emails: byh@mail.iap.ac.cn, ludr@mail.iap.ac.cn

Drop size distribution (DSD) is crucial for studying the microphysical properties of precipitation. Marshall and Palmer (1948) measured the mean distribution spectrum (M-P distribution) of raindrops in detail. Ulbrich (1983) proposed a three-parameter Gamma distribution function for the raindrop size distribution, which is widely used as the main method for characterizing the DSD in mesoscale models. Milbrandt and Yau (2005) showed that cloud and precipitation properties simulated with fixed shape parameters are highly sensitive to the values of the shape parameter since the shape parameter plays an important role in determining sedimentation and microphysical growth rates. Notably, polarization radars make use of oblateness to measure the difference in backscatter reflectivity and propagation phase. A small error in the axis ratio can lead to significant errors in the estimated DSD and rainfall rates (Chandrasekar et al., 1988; Thurai and Bringi, 2005). Many researchers have studied the microphysical properties of different types of precipitation based on DSD (Tokay and Short, 1996; Bringi et al., 2003; Brandes et al., 2004; Williams et al., 2007; Thurai et al., 2016). Studying the microphysics of clouds and precipitation also drives improvements in numerical models (Lu et al., 2023; Zhu et al., 2024). It has been shown that the characteristics of DSD vary across time, region, and topography (Bringi et al., 2003; Kozu et al., 2006; Ulbrich and Atlas, 2007; Tokay et al., 2008; Bumke and Seltmann, 2012; Chakravarty and Raj, 2013). Therefore, it is necessary to continue rainfall observations in YBJ or other regions of the TP, both now and in the future.

Over the past few decades, DSD observations have been conducted over a variety of regions in China using various disdrometers (Chen et al., 2013, 2016; Wen, et al., 2016 Wen et al., 2017; Lyu et al., 2022; Lü et al., 2023). So far, precipitation information obtained on the TP through professional instruments is still very limited. Previous studies on clouds and precipitation on the TP mainly used satellite observations to statistically analyze the macroscopic characteristics of clouds (Fu et al., 2006; Ma et al., 2017). In recent years, some researchers have also studied the microphysical characteristics of precipitation and raindrops on the TP (Porcù et al., 2014; Chen et al., 2017; Chang et al., 2019; Wang et al., 2021). Chang et al. (2019) conducted aerial measurements during the third atmospheric science experiment on the TP and suggested that the significant diurnal variation in summer clouds and precipitation on the TP is caused by the intense solar radiation on the TP. Chen et al. (2017) analyzed the DSD characteristics of the hinterland of the TP using a 2nd generation OTT Particle Size Velocity (OTT Parsivel^2) disdrometer in Nagqu (4500 m elevation with a straight-line distance from YBJ of approximately 210 km). The DSD characteristics of stratiform rain were less affected by day–night changes, whereas those of convective rain exhibited significant day–night variations, with more small raindrops and fewer large raindrops at night compared to daytime. Wang et al. (2021) measured the raindrop size distribution with an OTT Parsivel^2 disdrometer in Medog (1275 m), located on the southeastern Tibetan Plateau. However, the fact that Medog is located to the south of the Himalayas deems this data unrepresentative of the precipitation characteristics of the hinterland of the TP.

At present, most research on the TP uses the OTT Parsivel^2 for droplet spectrum measurement, which has the advantages of low cost, easy installation, and convenient maintenance. However, previous studies have shown that compared to the two-dimensional video disdrometer (2DVD), OTT Parsivel^2 underestimates the number of small droplets and overestimates the number of large droplets (Tokay et al., 2013; Wen et al., 2016). The short continuous observation time and large instrumental errors are the main factors that constrain the acquisition of accurate DSD observation data on the TP. As the most accurate disdrometer currently available, the 2DVD is superior to OTT Parsivel^2 in terms of measurement accuracy for both small and large raindrops, and can measure the axis ratio of raindrops (Wen et al., 2016; Luo et al., 2021).

The Institute of Atmospheric Physics, Chinese Academy of Sciences (IAP, CAS) has established the Atmospheric Profiling Synthetic Observation System (APSOS) in YBJ (Lu et al., 2018). One of its main objectives is to detect data on clouds and precipitation over the TP and obtain statistical characteristics of raindrop spectra in the hinterland of the TP, which will be of great help in studying the microphysical processes of clouds and precipitation, further aiding the improvement the microphysical parameterizations in present-day weather and climate models. This study used a 2DVD to conduct fixed-point long-term continuous observations in the YBJ area. Our observations spanned 27 months and three rainy seasons from July 2021 to September 2022, which were not available in previous studies. The study of raindrop size distribution contributes to understanding the microphysical characteristics of precipitation, thereby improving quantitative precipitation estimation (QPE) (Wen et al., 2016, 2020; Chen et al., 2017; Wen et al., 2017), and enhancing the accuracy of numerical forecasting in the hinterland of the TP. The China Meteorological Administration has deployed C-band radar in Lhasa, Linzhi, Rikeze, and Nagqu, but due to the obstruction of high mountains, the effective detection range of the radar is greatly limited. Therefore, the detection advantage of precipitation satellites on the TP is extremely obvious. Currently, a dual-frequency precipitation radar (DPR) is mainly used for this purpose, which is a primary instrument aboard the Global Precipitation Measurement (GPM) Mission Core Observatory satellite. On 16 April 2023, China's first precipitation measurement satellite, FengYun-3G (FY-3G) was successfully launched, carrying a precipitation measurement radar (PMR), which will greatly promote the study of precipitation on the TP. The FY-3G PMR consists of a Ku-band precipitation radar (13.35 GHz) and a Ka-band precipitation radar (35.55 GHz), which, allows us to improve the precipitation retrieval algorithm for dual-frequency precipitation radars in the hinterland of the TP aboard the the FY-3G and GPM satellites.

Here, we analyze the microphysical characteristics of rainfall in the region, along with a statistical analysis of DSD parameters and the axis ratio. The remainder of this paper is organized as follows. The data and methodology adopted in this study are described in section 2. Section 3 presents the DSD properties of different rain rates and precipitation types. Section 4 obtains the empirical relationship between the equivalent reflectivity of Ka and Ku band radars and improves the precipitation inversion algorithm of TP hinterland dual-frequency precipitation radar. The summary and conclusion are provided in section 5.

2. Instruments and methods

2.1. *Instruments*

The YBJ Observatory is located in the town of YBJ, Damxung County, Lhasa City, Tibet Autonomous Region. It is backed by the Nyenchen Tanglha Mountains, with an elevation of 4300 m, a latitude and longitude of 30°05′N, and 90°33′E. The red star marker in Fig. 1 shows the location. The instruments used in this paper include the third-generation 2DVD developed by Joanneum Research, Austria, which has been set up at the YBJ Observatory, and a Total Rain Weighing Sensor (TRWS204).

The 2DVD used in present observations is a particle imaging system consisting mainly of two orthogonal high-speed line scan cameras with crossed optical paths, with an effective sampling area of 10 × 10 cm^2, which can obtain front and side profiles, drop velocities, precise time stamps, rain rate, drop size distribution, and other data (Huang et al., 2015). Small particles can be measured in the 2DVD more accurately than with the OTT $Parsivel^2$ (Zhang et al., 2011; Thurai et al., 2014), which is an advantage for this study.

To ensure the proper functioning of the 2DVD and the reliability of the acquired data, the calibration should be performed in strict accordance with the manufacturers' calibration steps after the installation of the instrument and whenever the lamps are replaced. Calibration is achieved by releasing calibration balls (0.5, 1.0, 1.5, 2, 3, 4, 5, 6, 8, and 10 mm in diameter). Schönhuber et al. (2007) concluded that the measurement accuracy of individual particles was determined by averaging 100 calibration sphere readings and that the results usually did not deviate from the established values by more than 1%. Diameter tests are conducted using calibration spheres of 0.5 mm and larger, while height and width ratios are assessed with calibration spheres of 2 mm and larger. The 2DVDs used in this study were calibrated at regular intervals, and the calibrated results were consistent with the findings reported by Schönhuber et al. (2007).

2.2. *Quality control of 2DVD data*

From July 2021 to September 2023, long-term and continuous fixed-location observations were conducted. The accuracy of the 2DVD is mainly affected by the strong wind interference and splash during measurement (Nešpor et al., 2000).

Considering the uniqueness of precipitation on the TP, we adopt the diameter terminal velocity model with an air density correction proposed by Atlas et al. (1973) as a filter to remove the raindrops with velocities outside the ±60% range. Figure 2a shows the relationship between the falling terminal velocity and particle size, with the diameter terminal velocity model and the ±60% range lines indicated.

In this study, samples with a total of less than 10 raindrops within a minute were also filtered out, including potential non-rainfall samples caused by flying insects entering the detection area (Tokay et al., 2013). After quality control, a total of 26980 1-minute precipitation samples was obtained to evaluate the effectiveness of instrument measurement and quality control of the 2DVD data.

Figures 2b and 2c show the comparison of the rain rate

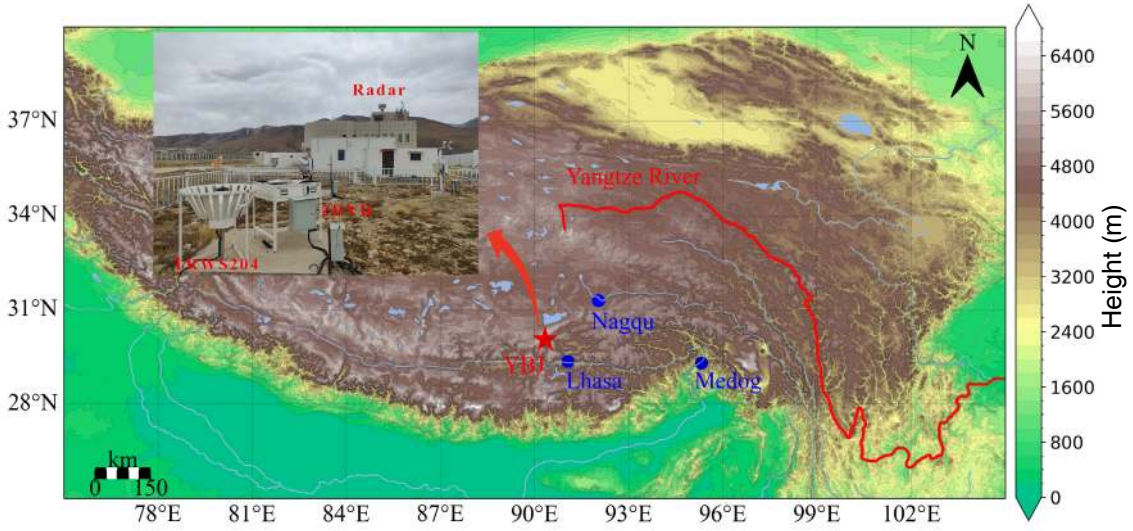

Fig. 1. Map of the YBJ Observatory (red star) and the other stations (blue circle), with the Yangtze River represented by a red line. The picture also shows actual shots of some instruments at the YBJ station.

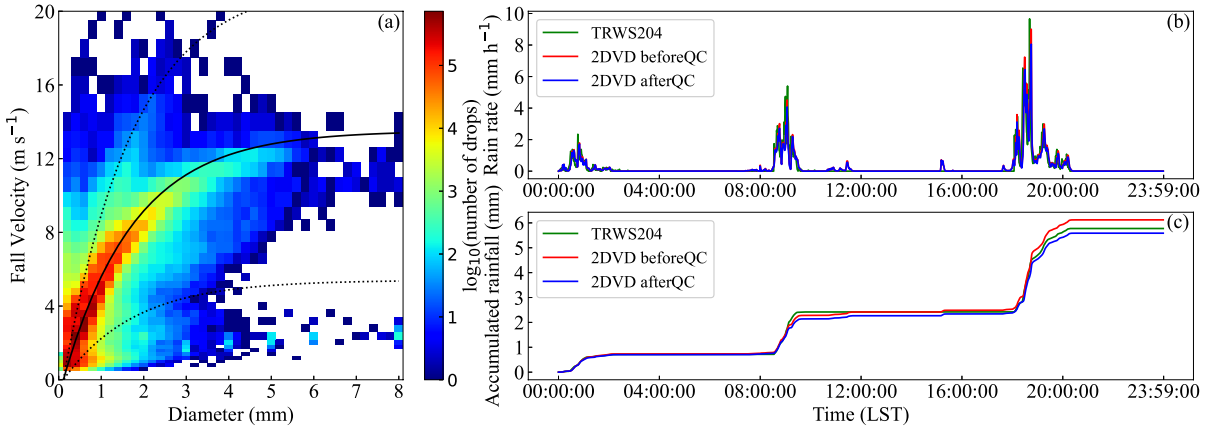

Fig. 2. (a) Heatmap of the number of raindrops with different particle sizes and terminal velocity classifications. The black solid line is the V-D empirical formula proposed by Atlas et al. (1973) after correcting for air density, and the dotted line represents the terminal velocity boundary of the ± 60% empirical formula. (b) Comparison of 2DVD pre- and post-quality control data and rain gauge rainfall rates and (c) accumulated rainfall. The solid green line is the rain gauge (TRWS204), the solid red line is before the 2DVD quality control and the solid blue line is after the quality control.

and accumulated rainfall calculated from DSD data measured by the 2DVD before and after quality control, and the data obtained from a rain gauge on 5 August 2021. The objective is to verify the effectiveness of quality control and further study the microphysical characteristics of precipitation in the YBJ area. The rain rate and accumulated rainfall from all three datasets are generally consistent. The 2DVD DSD data is also sensitive to low rain rates, although it slightly underestimates the peak rain rate. Schönhuber et al. (2007) suggested that for volumetric parameters such as rainfall, the rate of difference between the 2DVD and rain gauges compared to rainfall is typically less than 10%. Figure 2c shows that the deviation of the accumulated rainfall between the rain gauge data and the measurements before and after the quality control of 2DVD data at YBJ Station is 5.3 and 3.6%, respectively. The deviation between the 2DVD quality control data and the rain gauge data is well below 10%. Therefore, the revised data is of better quality.

2.3. *Calculation of DSD parameters*

In this paper, the raindrop diameters collected by the 2DVD are divided into 41 isometric particle size bins, and the velocities are divided into 41 non-isometric velocity bins (Cao et al., 2008). Therefore, the number of raindrop concentrations for the i-th particle size channel $N(D_i)$ (mm^{-1} m^{-3}) can be expressed as:

$$N(D_i) = \sum_{j=1}^{M_i} \frac{1}{\Delta t \Delta D V_j A_j}\,, \tag{1}$$

where D_i (mm) is the median equivalent volume diameter of the i-th particle size channel, and Δt (mm) is the effective sampling interval, set to 60 s in this study. A_j (m^2) is the effective sampling area, set to 0.01 m^2 in this study. ΔD (mm) is the bin size (0.2 mm) (Luo et al., 2021). M_i is the number of raindrops in the i-th particle size bin during the effective sampling time. V_j (m s^{-1})is the terminal fall speed for velocity class j.

When $N(D_i)$ is given, the rain rate R (mm h^{-1}), liquid water content W(g m^{-3}), total raindrop concentration N_T (m^{-3}), and radar reflectivity factor Z (mm^6 mm^{-3}) are calculated as follows:

$$R = \frac{6\pi}{10^4} \sum_{i=1}^{L} D_i^3 V_i N(D_i) \Delta D_i\,, \tag{2}$$

$$W = \frac{\pi \rho_w}{6000} \sum_{i=1}^{L} D_i^3 N(D_i) \Delta D_i\,, \tag{3}$$

$$N_T = \sum_{i=1}^{L} N(D_i) \Delta D_i\,, \tag{4}$$

$$Z = \sum_{i=1}^{L} D_i^6 N(D_i) \Delta D_i\,, \tag{5}$$

where L is the total number of bins and V_i is the end velocity of the raindrop at a particle size of D_i. ρ_w (1 g cm^{-3}) is the density of pure water.

It is widely accepted that using a three-parameter Gamma distribution function can effectively represent the distribution of the raindrop size distribution, which is expressed as:

$$N(D) = N_0 D^{\mu} \exp(-\Lambda D)\,, \tag{6}$$

where D (mm) is the raindrop diameter. N_0 (m^{-3} mm$^{-1-\mu}$) is the intercept parameter. μ is the shape parameter. Λ (mm^{-1}) is the slope parameter.

In this paper, we use the method of order moments to fit the parameters of the Gamma distribution function, and the n-th-order moment M_n is defined as follows (Tokay and Short, 1996):

$$M_N = \int_{D_{\min}}^{D_{\max}} D^n N(D)\,\mathrm{d}D\,. \tag{7}$$

The mass-weighted average diameter can be obtained using the method of order moments D_m (mm) and the normalized intercept parameter N_w ($\mathrm{m^{-3}\ mm^{-1}}$) (Bringi et al., 2003):

$$D_m = \frac{M_4}{M_3}\,, \tag{8}$$

$$N_w = \frac{4^4}{\pi\rho_w}\left(\frac{10^3 W}{D_m^4}\right). \tag{9}$$

The three parameters N_0, μ, and Λ of the gamma distribution function are fitted using the 2nd, 4th and 6th moments of the DSD observation, respectively (Zhang et al., 2003).

3. Analysis of rainfall characteristics

3.1. *Drop size distribution characteristics for different rain rates*

Existing research has shown that precipitation with different rain rates can exhibit distinct DSD characteristics, and it is necessary to study the classification of precipitation by rain rate in Tibetan areas. This paper uses the classification proposed by Chen et al. (2017) in Nagqu to classify precipitation into five classes in the YBJ: (1) R1: $0 < R < 0.1$ mm $\mathrm{h^{-1}}$, (2) R2: $0.1 \leqslant R < 1$ mm $\mathrm{h^{-1}}$, (3) R3: $1 \leqslant R < 5$ mm $\mathrm{h^{-1}}$, (4) R4: $5 \leqslant R < 10$ mm $\mathrm{h^{-1}}$, (5) R5: $R \geqslant 10$ mm $\mathrm{h^{-1}}$. As shown in Fig. 3a, R1 and R2 have the longest total rainfall duration, accounting for 86% of the total rainfall time. R3 contributes the most to the total rainfall, representing approximately 49%. Overall, there is a 99% probability of light rain

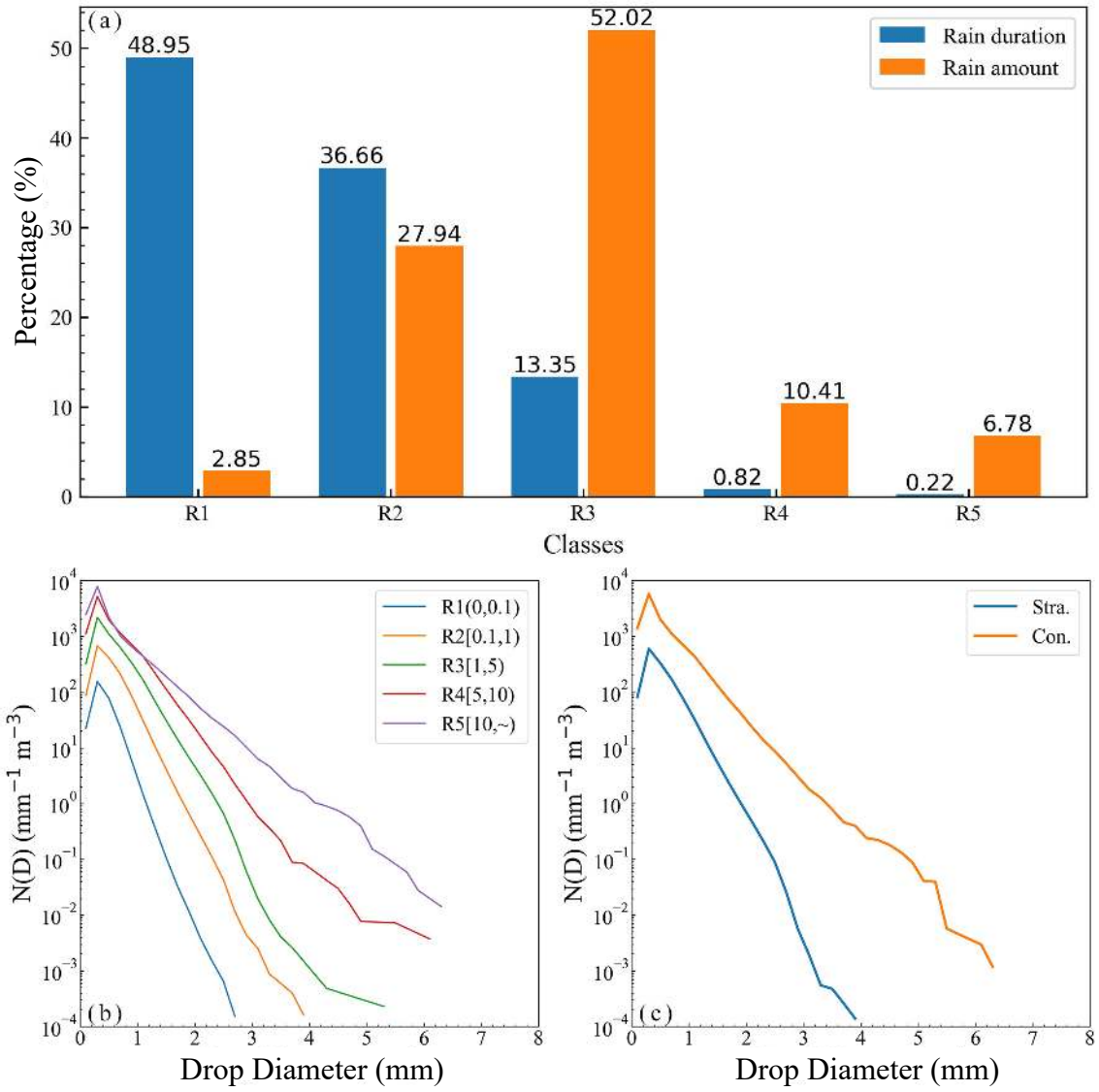

Fig. 3. Average raindrop size spectra. (a) Histograms of accumulated rain amount (orange) and rain duration (blue) for the five rain rate classes. (b) Average raindrop size spectra for five different rain rates. (c) Average raindrop size spectra for stratiform and convective rain.

(R< 5 mm h^{-1}) occurring in YBJ.

Figure 3b shows the average spectra of the five rain rates in the YBJ. The DSD spectra for different classes are similar. When D > 1 mm, the concentration and spectral width of raindrops increase with the increase in rain rate. The raindrop spectra of the five precipitation grades all exhibit singular peaks, and the maximum concentration of the droplet particles occurs at a particle diameter of 0.3 mm. The concentration of small raindrops in R5 is close to, or even slightly less than, that in R4. This phenomenon may be attributed to the 2DVD being affected by errors resulting from the oversampling of small raindrops caused by wind-induced turbulence near the optical camera and the splash contamination (Kruger and Krajewski, 2002; Chang et al., 2009).

The integral rain parameters calculated from the average DSD are shown in Table 1. As the rainfall rate increases, the liquid water content W, total raindrop concentration N_T, radar reflectivity factor Z, and mass-weighted mean diameter D_m calculated from the average spectrum also increase.

3.2. *Drop size distribution characteristics of stratiform and convective rain*

To study the characteristics of the raindrop spectra of different types of precipitation, precipitation is typically categorized into two main groups, stratiform rain and convective rain. The formation mechanisms of these two types of precipitation are different, resulting in different microphysical characteristics (Stout and Mueller, 1968). Therefore, studying the microphysical characteristics of precipitation requires classifying precipitation in advance (Tokay and Short, 1996; Bringi et al., 2003; Chen et al., 2013, 2017; Wen et al., 2020). Many studies have used ground-based disdrometer data to classify stratiform and convective rain based on rain rate. Chen et al. (2017) proposed a classification method based on the Bringi et al. (2003) method, which relies on the rainfall rate (R) and its standard deviation (σR). This method requires ensuring that the first and second five minutes are continuous: (1) $\sigma R \leqslant 1.5$ mm h^{-1} is classified as stratiform and (2) $R \geqslant 5$ mm h^{-1} and $\sigma R \geqslant 1.5$ mm h^{-1} is classified as convective. We identified 19272 (98.4%) 1-min data as stratiform and 310 (1.6%) 1-min data as convective. The statistical results show that stratiform precipitation accounts for 80% of the total rainfall, while convective rainfall accounts for 20%.

The average raindrop spectra for the stratiform rain and convective rain are presented in Fig. 3c. The integral rain parameters calculated from the average raindrop spectra for stratiform and convective rain are provided in Table 2. The mean spectra for both stratiform and convective rain exhibit peaks at a particle size of 0.3 mm, although the maximum drop size varies, being 3.9 mm for stratiform and 6.3 mm for convective rain.

3.3. $D_m - N_w$ *distribution characteristics*

The frequency histograms showing the occurrence of D_m and lgN_w for stratiform and convective rain types, along with their mean, standard deviation, and skewness, are also presented in Fig. 4. The D_m values for stratiform and convection rain fall within the range of 0.4–1.1 mm and 0.8–1.6 mm, respectively, with average values of 0.81 mm and 1.47 mm. The lgN_w values for stratiform rain are concentrated between 3.0 and 4.2, while for convective rain, they are concentrated between 3.3 and 4.8, resulting in a higher STD for convective rain compared to stratiform rain. The histograms of D_m and lgN_w for convective rain tend to shift toward larger values relative to that of the stratiform rain histogram, indicating that convective rain exhibits higher D_m and lgN_w values.

To compare the mean values of D_m and lgN_w with those of other climate regimes, Fig. 5 gives the $D_m - \lg N_w$ distribution for stratiform and convective rain. The boundary between stratiform rain and convective rain, as defined by Bringi et al. (2003), is also given. The clusters, as defined by Bringi et al. (2003), correspond to maritime- and continental-like convective rain. These are overlaid on a scatterplot with two black rectangles. The figure also shows the results for other regions of the TP (Nagqu and Medog) and eastern China. We further conduct a fitting analysis of the $D_m - \lg N_w$ relationship for stratiform and convective rain as follows:

Table 1. Integral parameters obtained from the calculation of the average raindrop size spectra for the five rain rates.

	Sample size	$N_t\left(\mathrm{m}^{-3}\right)$	Z(dBZ)	W(g m^{-3})	D_m(mm)	lgN_w	μ	Λ(mm^{-1})
R1	13207	57.16	4.75	0.003	0.67	1.89	1.42	7.96
R2	9891	304.03	18.64	0.031	0.89	2.40	0.97	5.51
R3	3602	969.25	27.39	0.137	1.07	2.72	0.94	4.60
R4	221	2201.34	35.34	0.389	1.31	2.83	–0.33	2.74
R5	59	3094.45	43.21	0.757	1.93	2.45	–0.64	1.76

Table 2. Integral parameters obtained from the calculation of average raindrop spectra for stratiform rain and convective rain.

	Sample size	$N_t\left(\mathrm{m}^{-3}\right)$	Z(dBZ)	W(g m^{-3})	D_m(mm)	lgN_w	μ	Λ(mm^{-1})
Stra.	19272	261.25	19.68	0.030	0.98	2.23	0.76	4.85
Con.	310	2388.60	38.51	0.466	1.51	2.65	–0.87	2.01

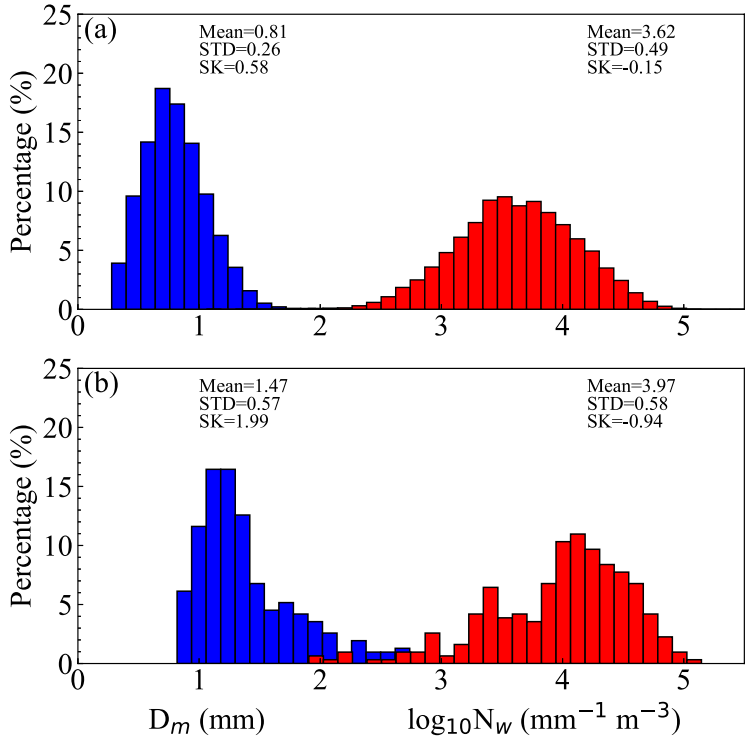

Fig. 4. The bar distribution of D_m and lgN_w for (a) stratiform rain and (b) convective rain. The mean (Mean), standard deviation (STD), and skewness (SK) for both parameters are given in the figure.

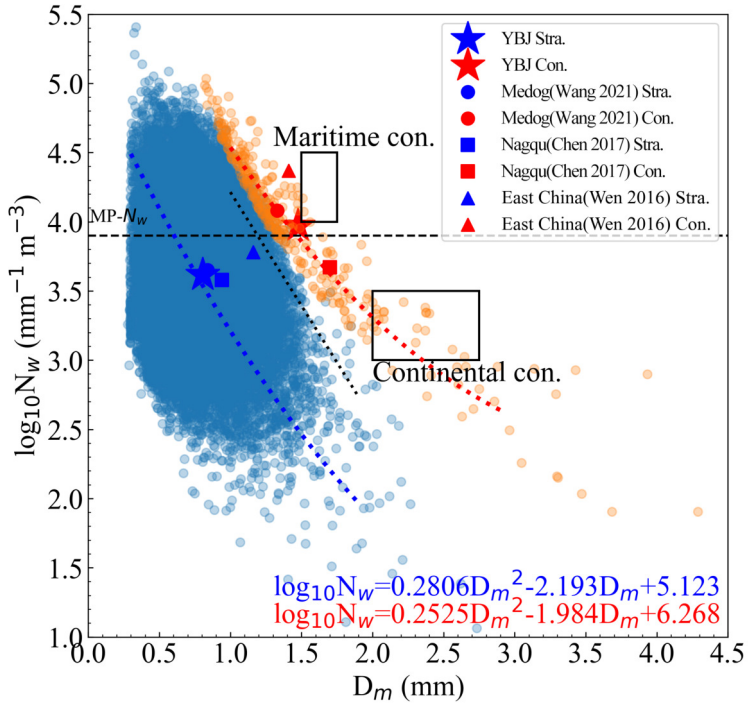

Fig. 5. The distribution of D_m–lgN_w for stratiform rain (blue) and convective rain (red). The square marks represent the results from YBJ, while the circular marks show the result from Medog (Wang et al., 2021), the star marks represent Nagqu (Chen et al., 2017), and the triangular marks correspond to East China (Wen et al., 2016). The black rectangles correspond to the maritime and continental convective clusters defined by Bringi et al. (2003), and the dotted line denotes the stratiform cases.

$$\text{Stra.:}\ \lg N_w = 0.2806 D_m^2 - 2.193 D_m + 5.123\ , \qquad (10)$$

$$\text{Con.:}\ \lg N_w = 0.2525 D_m^2 - 1.984 D_m + 6.268\ . \qquad (11)$$

It is obvious that the convective rain of YBJ, Medog, and Nagqu are all near the line.

Our results indicate that the summer convective rain in YBJ exhibits more maritime characteristics, while its stratiform rain is very similar to other regions. The convective rain in YBJ is comparable to that in the other areas. However, there are some differences. Unlike the abundant warm and humid atmospheric conditions in Medog and eastern China (Wang et al., 2021), the YBJ and Nagqu regions have high altitudes and are relatively dry. Research conducted by Chang et al. (2019) suggests that summer clouds on the TP may primarily consist of mixed-phase cumulus clouds that formed due to intense solar heating, and the 0°C-layer bright band is lower than that in East China. This could result in a relatively shorter condensational growth distance for raindrops, potentially leading to a higher number of small raindrops. However, further research is needed to validate these observational findings.

3.4. μ–Λ *relationship*

The μ–Λ relationship can provide insights into the DSD characteristics of different regions, as demonstrated in previous studies (Zhang et al., 2003; Chen et al., 2013; Thurai et al., 2014; Wen et al., 2016). The YBJ region is a representative area in the TP hinterland, making it essential to study the μ–Λ relationship. We employ the method described in Chen et al. (2017) to filter out data with particle numbers fewer than 300. This not only improves data dispersion but also helps eliminate, to some extent, unreasonable data resulting from measurement and calculation errors. A least squares fit was employed to derive the μ–Λ relationship:

$$\Lambda = 0.03632\mu^2 + 1.608\mu + 3.472\ , \qquad (12)$$

and

$$\mu = -0.005084\Lambda^2 + 0.579\Lambda - 1.521\ . \qquad (13)$$

The fitted coefficients are similar to the results of previous studies (Cao et al., 2008; Chen et al., 2017; Wang et al., 2021), but they are not identical. Figure 6a shows the YBJ area's μ–Λ scatterplot and gives the fitted curves. Figure 6b is a comparison plot of the μ–Λ relationship. In this case, the values of Chen et al. (2017) and Wang et al. (2021) were observed using the OTT Parsivel^2 in Nagqu and Medog, respectively; while those of Cao et al. (2008) were observed using the 2DVD in Oklahoma. The fitted relationship of YBJ is closer to the relationship reported by Cao et al. (2008) compared to other relationships. For a given Λ, the relationship proposed by Chen et al. (2017) and Wang et al. (2021) has higher μ values compared to our relationship. Previous studies (Tokay et al., 2013; Wen et al., 2016) have shown that higher μ values can be partially attributed to the underestimation of small drops by the OTT Parsivel^2. Similarly, with the same Λ value, the m value of YBJ is smaller, indicating a higher concentration of small raindrops in the YBJ. As Λ increases, the three curves in TP tend to become more scattered. In addition to measurement errors resulting from the use of different instruments, this scattering may also be influenced by the unstable convective activity in the boundary layer of the TP.

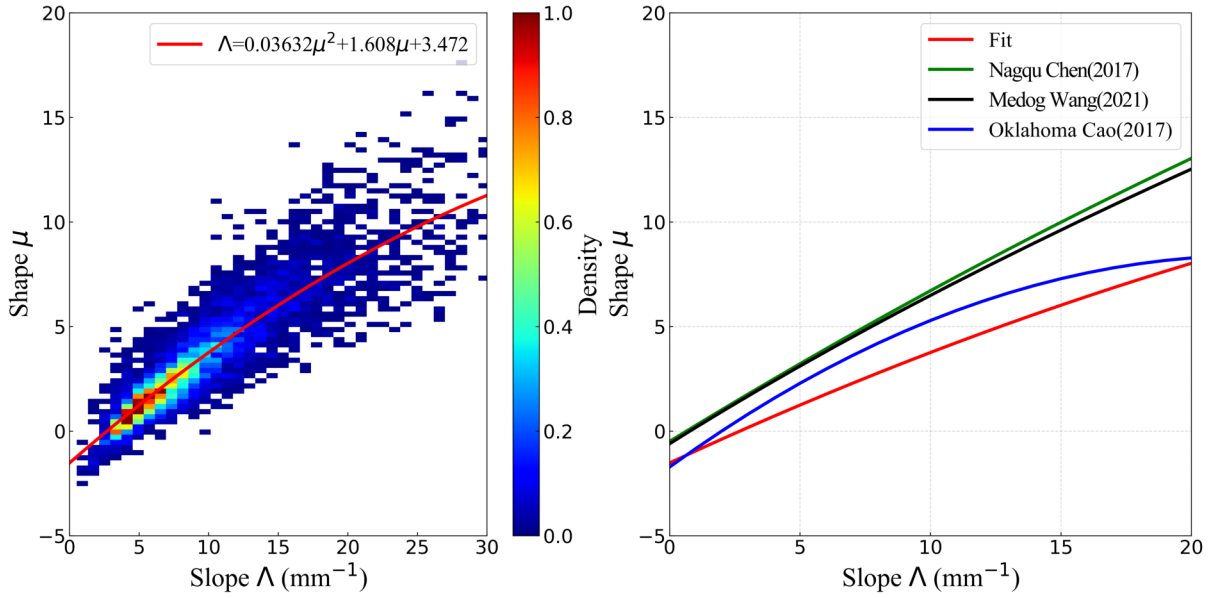

Fig. 6. Scatterplots of μ–Λ with DSD. (a) The μ–Λ relationship scatter density heatmap. The red solid line represents the μ–Λ relationship fitted using the least squares method. (b) Comparison plot of the μ–Λ relationship. The green, black, and blue solid lines represent the μ–Λ relationship for Chen et al. (2017) in Nagqu, Wang et al. (2021) in Medog, and Cao et al. (2008) in the Oklahoma report, respectively.

3.5. *Axis ratio*

The shape of a raindrop during its fall is nearly an oblate spheroid, with its symmetrical axis closely aligned with its vertical axis, and there is a monotonic relationship between its axis ratio and raindrop size (Thurai and Bringi, 2005). Polarimetric radar uses the axis ratio to measure backscattering and propagation phase differences, so the shape parameters of the raindrops play a crucial role in retrieving rain DSD by polarimetric radar and in the quantitative estimation of precipitation. In this paper, we use the 2DVD to measure the axis ratio of raindrop particles on the TP, which can improve the application of polarimetric radar in this region.

Figure 7a shows the distribution information for the number of raindrops at 0.2 mm diameter intervals and 0.02 axis ratio intervals. The white error bars indicate the mean value of the axis ratio at each equivalent particle size interval and their respective standard deviations ($\pm 1\sigma$). The detection of axis ratios for raindrop particles with a particle diameter of less than 0.5 mm is inaccurate and is generally attributed to the limitations of the instrument itself (Kim et al., 2016; Luo et al., 2021). We have adopted the recommendation of Chang et al. (2019), who suggested that particles with diameters less than 0.5 mm are nearly spherical (with an axis ratio close to 1). Figure 7a shows that the measured axis ratio of raindrop particles with large particle diameters oscillates as the particle diameter increases. This subset of the raindrop particles has fewer measured samples and is more susceptible to wind influence. Therefore, only particles with particle diameters less than 3 mm are considered for fitting to minimize the impact of clutter on the fitted relationship.

The fourth-order polynomial relationship for the mean axis ratio of raindrops in the YBJ region of the TP is given by:

$$\frac{b}{a} = -7.745\times10^{-4}D^4 + 9.67\times10^{-3}D^3 - 4.026\times10^{-2}D^2 + 1.935\times10^{-2}D + 1.001\,, \quad (14)$$

where a and b are the long and short axes of the raindrop, respectively, and D represents the equivalent diameter of the raindrop.

In Fig. 7b, the relationship between the equivalent diameter of raindrops and the axis ratio in the YBJ is plotted as a red solid line, and it is compared to axis ratio relationships from three previous studies (Beard and Chuang, 1987; Wen et al., 2017; Luo et al., 2021). This comparison reveals that as the equivalent diameter increases, the raindrop shapes in the YBJ tend to approach that of a spheroid. This phenomenon may be influenced by factors such as low air density, low air buoyancy, and horizontal winds in plateau areas.

3.6. *Rainfall estimation relationships*

This section proposes a radar-based quantitative precipitation estimation (QPE) algorithm based on the DSD characteristics observed during the three rainy seasons (2021–23) at the YBJ station. The Z-R relationship in the form of a power law function ($Z = aR^b$) is widely used for QPE (Zhang et al., 2001; Brandes et al., 2002; Ryzhkov et al., 2005; Lee, 2006; Cao et al., 2010). Variations in atmospheric dynamics and microphysical processes across different regions can alter the coefficients of the Z-R relationship (Tokay et al., 2008). Table 3 provides the fitted Z-R relationships for stratiform and convective rain.

Figure 8 shows the scatterplots and fits of the Z–R rela-

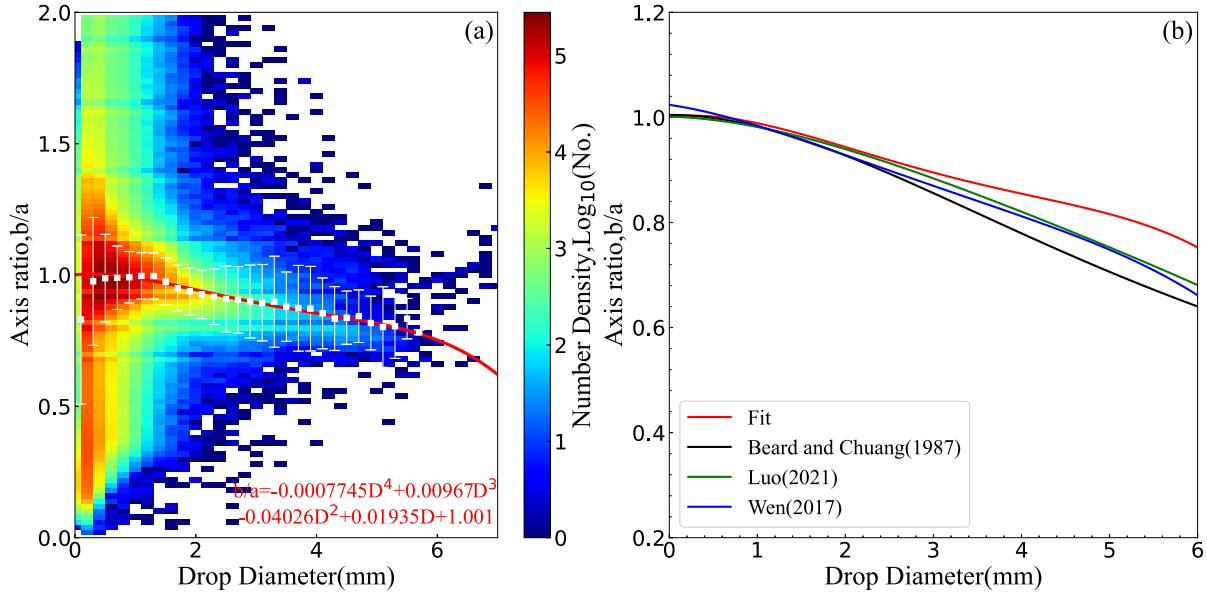

Fig. 7. Distribution of the drop number density (log scale) as a function of drop diameter and axis ratio (b/a). (a) The distribution plot of raindrop number density with equivalent diameter and axis ratio, with the mean and error indicated by the white error bars and the red solid line showing the fitted relationship between diameter and axis ratio. (b) A comparison of the diameter and axis ratio relationship from previous studies and the relationship in YBJ.

tionship for stratiform rain and convective rain. The Z–R relationship for YBJ is on the left side of Medog, indicating that the rainfall rate of YBJ is lower than that of Medog at the same Z value. The Z–R relationship of stratiform rain in YBJ and Nagqu is highly consistent. For a given R-value, the Z of convective rain in YBJ is greater. This may be related to the abundance of small raindrops in YBJ.

4. Rainfall retrieval application with dual-frequency radar

Based on the above analysis results concerning the statistical characteristics of the YBJ DSD, we will generalize and apply them to improve the rainfall retrieval algorithms of the satellite dual-frequency precipitation radar in the hinterland of the TP. It should be noted that the data from FY-3G has been made publicly available. However, the current accumulation of rainfall data in the hinterland of the TP, as documented by FY-3G, is very limited. Nevertheless, we will try to provide some rainfall retrieval algorithms for the FY-3G data using the long-term 2DVD data shown in previous sections as a preliminary result. The effective radar reflectivity factor Z_e (mm^6 mm^{-3}) for a specific wavelength can be expressed as follows:

$$Z_e = \frac{\lambda^4}{\pi^5 |K_w|^2} \sum_{D_{\min}}^{D_{\max}} N(D_i)\sigma(D_i,\lambda)\Delta D_i \,, \tag{15}$$

where λ is the radar wavelength and $\sigma(D_i,\lambda)$ is the backscattering cross-section of a water drop with diameter D_i, which is directly calculated according to Mie theory. $|K_w|^2$ is the dielectric factor, which is related to the complex refractive index of water and is taken to be 0.93 by convention (Zhang et al., 2001). The Z_e–R relationship of Ka band radar reflectivity (Z_{Ka}) and Ku band radar reflectivity (Z_{Ku}), as calculated by the T-matrix (Mishchenko et al., 1996) and rainfall rate was fitted. The results are presented in Table 4.

The weak precipitation with rainfall intensity less than 1 mm h^{-1} in the YBJ area accounts for nearly 86% of the total precipitation time (Fig. 3a). Millimeter wave cloud radar has a higher detection ability for non-precipitating and weak precipitating clouds than centimeter wave weather radar due to its short wavelength. Its high sensitivity and spatial resolution enable it to effectively detect the structure and physical characteristics of small particles (Kollias et al., 2007). Therefore, we use the difference in the radar equivalent

Table 3. *Z-R* fitting relationships of stratiform and convective rain.

Type	Z–R Relationship
Stratiform	$Z = 185.48R^{1.33}$
Convective	$Z = 72.02R^{1.96}$

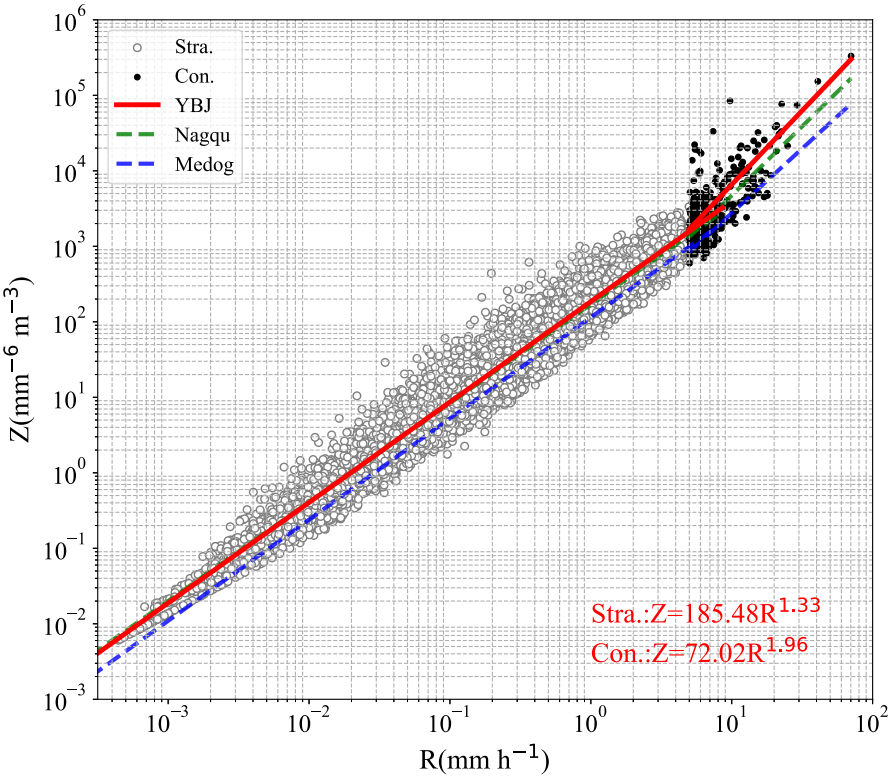

Fig. 8. *Z-R* logarithmic distributions for stratiform rain (gray circles) and convective rain (black dots), along with their fitted relationships shown as solid red lines. In addition, the green and blue lines represent the Z–R relationship of Nagqu and Medog, respectively (Wu and Liu, 2017; Wang et al., 2021).

reflectivity factor between two frequencies (dual-frequency ratio referred to as DFR) of the FY-3G PMR (DPR), as well as the radar reflectivity at the Ku or Ka bands to estimate the parameters N_w and D_m, and then derive the rainfall rate.

The DFR (dB) is defined as:

$$\mathrm{DFR} = 10\lg(Z_{\mathrm{Ku}}/Z_{\mathrm{Ka}}) \,, \tag{16}$$

where Z_{Ku} and Z_{Ka} are the radar equivalent reflectivity factors at the Ku and Ka frequencies obtained from Eq. (15), respectively. Previous research has shown that when the DFR is positive, there is a one-to-one relationship between the DFR and D_m, while when the DFR is negative, one DFR value corresponds to two D_m values (Chen et al., 2017; Wang et al., 2021). Figure 9a indicates that due to the small diameter of raindrops in YBJ, there is still a dual value problem in this study. To avoid the dual value problem, this study adopted Liao and Meneghini (2019) modified DFR (DFR*) method in Fig. 9b. The DFR* (dB) is defined as:

$$\mathrm{DFR}* = 10\lg(Z_{\mathrm{Ku}}) - \gamma 10\lg(Z_{\mathrm{Ka}}) \,, \tag{17}$$

where γ is a scale factor with a value ranging from 0 to 1 (Liao and Meneghini, 2019). The γ for this study is taken as 0.7. We also used Z_e to obtain the empirical relationship of D_m. To eliminate scatter, the D_m–Z_e scatterplots for the data sets with $N_T > 300$ in YBJ are shown in Figs. 9c and 9d. D_m tends to increase with the increase of Z_e. We found that D_m was highly correlated with Z_e. Using a least squares fitting, we derive the following quadratic polynomial relationship:

$$D_m = 7.116\times10^{-4}Z_{\mathrm{Ku}}^2 + 6.15\times10^{-3}Z_{\mathrm{Ku}} + 0.4218 \,, \tag{18}$$

$$D_m = 7.031\times10^{-4}Z_{\mathrm{Ka}}^2 + 4.86\times10^{-3}Z_{\mathrm{Ka}} + 0.4261 \,. \tag{19}$$

Table 4. Fitting parameters for the $Z_e - R$ relationship.

$Z_e = aR^b$	a	b	R^2
Ku	91.17	2.08	0.91
Ka	387.38	1.05	0.80

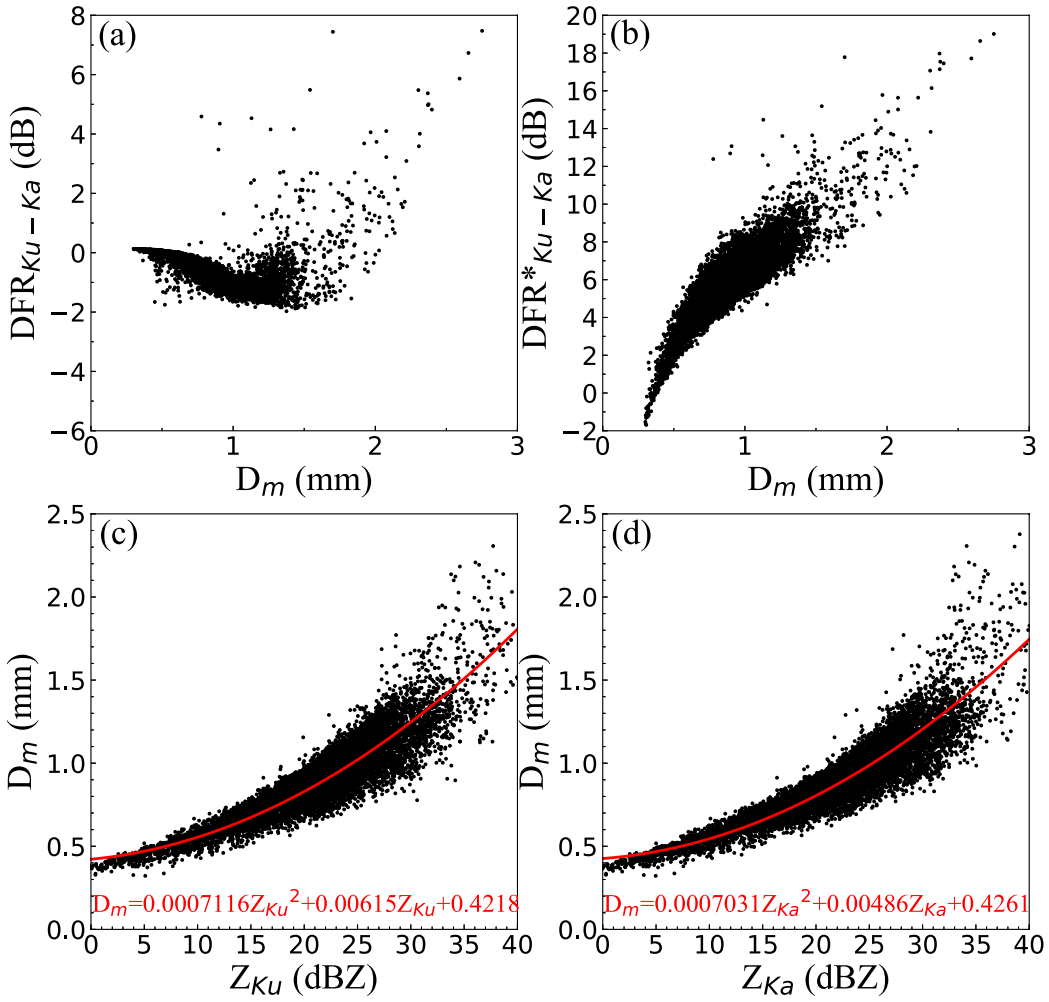

Fig. 9. Scatterplots showing the relationships of D_m with DFR, DFR (*), and Z_e. The top panels show the relationship between D_m and (a) the dual-frequency ratio (DFR) and (b) the modified DFR (DFR*). Scatterplots of D_m and Z_e in the (b) Ku and (c) Ka bands. The solid red line represents the fitted curve.

Because D_m and N_w are related, the empirical D_m–N_w relationship for stratiform and convective rain can be established as shown in Eqs. (10) and (11). As long as D_m and N_w are exported, the given μ can be used to reconstruct the DSD and ultimately estimate the rainfall rate (Chen et al., 2017).

5. Summary and Conclusion

This paper uses a 2DVD to analyze the microphysical characteristics of raindrops in precipitation, establishing a valuable set of cloud precipitation research and quantitative precipitation estimation models for the TP hinterland.

The microphysical characteristics of precipitation in YBJ suggest that convective rain exhibits more maritime characteristics compared to Nagqu. Convective rain with maritime characteristics is mainly characterized by a high numerical concentration of small raindrop sizes, predominantly generated within mixed-phase and warm clouds. The main source of water vapor in YBJ during summer is the warm and humid airflow transported from the Bay of Bengal to Lhasa. The airflow is obstructed by the mountains, and the uplift can easily cause terrain rain. These factors collectively result in the predominantly maritime nature of convective rain in YBJ. Additionally, the prevalent cloud formations over the TP during summer, characterized by mixed-phase cumulus clouds due to strong solar heating, contribute to the unique characteristics of summer convective rain in YBJ.

The main findings are as follows:

(1) The DSD was divided into five rainfall rate categories. A comparison of the spectral shape and width of the five average DSDs revealed that the average spectral shape is similar for different rain rates, with the spectral width increasing with rain rate. Statistical results indicate that 86% of the precipitation in YBJ falls into the weak precipitation category (R< 1 mm h^{-1}).

(2) Precipitation was classified into convective and stratiform types. YBJ exhibited similar D_m and lgN_w values to those in North China, resembling those documented by Nagqu and Medog for stratiform precipitation. It was found that convective rain could be identified as maritime-like and was characterized by a high numerical concentration of small raindrop sizes. We conducted the fitting analysis for the D_m–lgN_w relationship of stratiform and convective precipitation and found the mean values of YBJ, Medog, and Nagqu are all close to the lines.

(3) We derived empirical second-degree polynomials of the μ–Λ relationship in YBJ. For a given Λ, the μ value in this study is less than that derived from Nagqu. This paper also gives the relationship between the equivalent diameter and axis ratio of raindrops in the YBJ. Compared to low-altitude areas, the raindrop shapes in YBJ are closer to spherical as the equivalent particle diameter increases.

(4) We derived Z–R relationships for stratiform and convective rain and compared them with Nagqu and Medog. Convective rain in YBJ exhibited greater Z-values for a given R-value. Rainfall estimation algorithms, Z_{Ka}–R and Z_{Ku}–R were derived and discussed in terms of improving the precipitation inversion algorithm for the TP hinterland's dual-frequency precipitation radar. In addition, we used a modified DFR to improve the FY-3G (or GPM DPR) rainfall retrieval algorithm over the TP.

Acknowledgements. The authors would like to thank Prof. Congzeng HAN for polishing the article and Prof. Yuejian XUAN for the 2DVD calibration. The authors thank the reviewers for their great help on the article during its review progress. This research was funded by the second Tibetan Plateau Scientific Expedition and Research Program (2019QZKK0604).

REFERENCES

Atlas, D., R. C. Srivastava, and R. S. Sekhon, 1973: Doppler radar characteristics of precipitation at vertical incidence. *Rev. Geophys.*, **11**, 1–35, https://doi.org/10.1029/RG011i001p00001.

Beard, K. V., and C. Chuang, 1987: A new model for the equilibrium shape of raindrops. *J. Atmos. Sci.*, **44**, 1509–1524, https://doi.org/10.1175/1520-0469(1987)044<1509:Anmfte>2.0.Co;2.

Brandes, E. A., G. F. Zhang, and J. Vivekanandan, 2002: Experiments in rainfall estimation with a polarimetric radar in a subtropical environment. *J. Appl. Meteorol.*, **41**, 674–685, https://doi.org/10.1175/1520-0450(2002)041<0674:Eirewa>2.0.Co;2.

Brandes, E. A., G. F. Zhang, and J. Vivekanandan, 2004: Drop size distribution retrieval with polarimetric radar: Model and application. *J. Appl. Meteorol.*, **43**, 461–475, https://doi.org/10.1175/1520-0450(2004)043<0461:Dsdrwp>2.0.Co;2.

Bringi, V. N., V. Chandrasekar, J. Hubbert, E. Gorgucci, W. L. Randeu, and M. Schoenhuber, 2003: Raindrop size distribution in different climatic regimes from disdrometer and dual-polarized radar analysis. *J. Atmos. Sci.*, **60**, 354–365, https://doi.org/10.1175/1520-0469(2003)060<0354:Rsdidc>2.0.Co;2.

Bumke, K., and J. Seltmann, 2012: Analysis of measured drop size spectra over land and sea. *International Scholarly Research Notices*, **2012**, 296575, https://doi.org/10.5402/2012/296575.

Cao, Q., G. F. Zhang, E. Brandes, T. Schuur, A. Ryzhkov, and K. Ikeda, 2008: Analysis of video disdrometer and polarimetric radar data to characterize rain microphysics in oklahoma. *J. Appl. Meteorol. Climatol.*, **47**, 2238–2255, https://doi.org/10.1175/2008jamc1732.1.

Cao, Q., G. F. Zhang, E. A. Brandes, and T. J. Schuur, 2010: Polarimetric radar rain estimation through retrieval of drop size distribution using a bayesian approach. *J. Appl. Meteorol. Climatol.*, **49**, 973–990, https://doi.org/10.1175/2009jamc2227.1.

Chakravarty, K., and P. E. Raj, 2013: Raindrop size distributions and their association with characteristics of clouds and precipitation during monsoon and post-monsoon periods over a tropical Indian station. *Atmospheric Research*, **124**, 181–189, https://doi.org/10.1016/j.atmosres.2013.01.005.

Chandrasekar, V., W. A. Cooper, and V. N. Bringi, 1988: Axis ratios and oscillations of raindrops. *J. Atmos. Sci.*, **45**, 1323–1333, https://doi.org/10.1175/1520-0469(1988)045<1323:Araoor>2.0.Co;2.

Chang, W. Y., T.-C. C. Wang, and P.-L. Lim, 2009: Characteristics

of the raindrop size distribution and drop shape relation in typhoon systems in the western pacific from the 2D video disdrometer and NCU C-band polarimetric radar. *J. Atmos. Oceanic Technol.*, **26**, 1973–1993, https://doi.org/10.1175/2009jtecha1236.1.

Chang, Y., X. L. Guo, J. Tang, and G. X. Lu, 2019: Aircraft measurement campaign on summer cloud microphysical properties over the Tibetan Plateau. *Scientific Reports*, **9**, 4912, https://doi.org/10.1038/s41598-019-41514-5.

Chen, B. J., J. Yang, and J. P. Pu, 2013: Statistical characteristics of raindrop size distribution in the meiyu season observed in eastern China. *J. Meteor. Soc. Japan Ser. II*, **91**, 215–227, https://doi.org/10.2151/jmsj.2013-208.

Chen, B. J., J. Wang, and D. L. Gong, 2016: Raindrop size distribution in a midlatitude continental squall line measured by thies optical disdrometers over East China. *J. Appl. Meteorol. Climatol.*, **55**, 621–634, https://doi.org/10.1175/jamc-d-15-0127.1.

Chen, B. J., Z. Q. Hu, L. P. Liu, and G. F. Zhang, 2017: Raindrop size distribution measurements at 4,500 m on the Tibetan plateau during TIPEX-III. *J. Geophys. Res.*, **122**, 11 092–11 106, https://doi.org/10.1002/2017jd027233.

Fu, Y. F., G. S. Liu, G. X. Wu, R. C. Yu, Y. P. Xu, Y. Wang, R. Li, and Q. Liu, 2006: Tower mast of precipitation over the central Tibetan Plateau summer. *Geophys. Res. Lett.*, **33**, L05802, https://doi.org/10.1029/2005gl024713.

Huang, G.-J., V. N. Bringi, D. Moisseev, W. A. Petersen, L. Bliven, and D. Hudak, 2015: Use of 2D-video disdrometer to derive mean density–size and Z_e–SR relations: Four snow cases from the light precipitation validation experiment. *Atmospheric Research*, **153**, 34–48, https://doi.org/10.1016/j.atmosres.2014.07.013.

Kim, H.-L., M.-K. Suk, H.-S. Park, G.-W. Lee, and J.-S. Ko, 2016: Dual-polarization radar rainfall estimation in Korea according to raindrop shapes obtained by using a 2-D video disdrometer. *Atmospheric Measurement Techniques*, **9**, 3863–3878, https://doi.org/10.5194/amt-9-3863-2016.

Kollias, P., E. E. Clothiaux, M. A. Miller, B. A. Albrecht, G. L. Stephens, and T. P. Ackerman, 2007: Millimeter-wavelength radars: New frontier in atmospheric cloud and precipitation research. *Bull. Amer. Meteor. Soc.*, **88**, 1608–1624, https://doi.org/10.1175/bams-88-10-1608.

Kozu, T., K. K. Reddy, S. Mori, M. Thurai, J. T. Ong, D. N. Rao, and T. Shimomai, 2006: Seasonal and diurnal variations of raindrop size distribution in asian monsoon region. *J. Meteor. Soc. Japan Ser. II*, **84A**, 195–209, https://doi.org/10.2151/jmsj.84A.195.

Kruger, A., and W. F. Krajewski, 2002: Two-dimensional video disdrometer: A description. *J. Atmos. Oceanic Technol.*, **19**, 602–617, https://doi.org/10.1175/1520-0426(2002)019<0602:Tdvdad>2.0.Co;2.

Lee, G. W., 2006: Sources of errors in rainfall measurements by polarimetric radar: Variability of drop size distributions, observational noise, and variation of relationships between *R* and polarimetric parameters. *J. Atmos. Oceanic Technol.*, **23**, 1005–1028, https://doi.org/10.1175/jtech1899.1.

Liao, L., and R. Meneghini, 2019: A modified dual-wavelength technique for Ku- and Ka-band radar rain retrieval. *J. Appl. Meteorol. Climatol.*, **58**, 3–18, https://doi.org/10.1175/jamc-d-18-0037.1.

Lu, C. S., and Coauthors, 2023: Observational study of relationships between entrainment rate, homogeneity of mixing, and cloud droplet relative dispersion. *Atmospheric Research*, **293**, 106900, https://doi.org/10.1016/j.atmosres.2023.106900.

Lu, D. R., W. L. Pan, and Y. N. Wang, 2018: Atmospheric profiling synthetic observation system in Tibet. *Adv. Atmos. Sci.*, **35**, 264–267, https://doi.org/10.1007/s00376-017-7251-7.

Luo, L., J. Guo, H. N. Chen, M. L. Yang, M. X. Chen, H. Xiao, J. L. Ma, and S. T. Li, 2021: Microphysical characteristics of rainfall observed by a 2DVD disdrometer during different seasons in Beijing, China. *Remote Sensing*, **13**, 2303, https://doi.org/10.3390/rs13122303.

Lü, J. J., Y. Zhou, Z. K. Fu, C. S. Lu, Q. Huang, J. Sun, Y. Zhao, and S. J. Niu, 2023: Variability of raindrop size distribution during a regional freezing rain event in the Jianghan plain of central China. *Adv. Atmos. Sci.*, **40**, 725–742, https://doi.org/10.1007/s00376-022-2131-1.

Lyu, J. J., H. W. Xiao, Y. C. Du, L. N. Sha, Y. Q. Deng, W. K. Jia, S. J. Niu, Y. Zhou, and G. Q. Pang, 2022: Variations of raindrop size distribution and radar retrieval in outer rainbands of typhoon mangkhut (2018). *Journal of Meteorological Research*, **36**, 500–519, https://doi.org/10.1007/s13351-022-1134-2.

Ma, Z. Q., Z. Shi, Y. Zhou, J. F. Xu, W. Yu, and Y. Y. Yang, 2017: A spatial data mining algorithm for downscaling TMPA 3B43 V7 data over the Qinghai–Tibet Plateau with the effects of systematic anomalies removed. *Remote Sensing of Environment*, **200**, 378–395, https://doi.org/10.1016/j.rse.2017.08.023.

Marshall, J. S., and W. M. K. Palmer, 1948: The distribution of raindrops with size. *J. Meteorol.*, **5**, 165–166, https://doi.org/10.1175/1520-0469(1948)005<0165:Tdorws>2.0.Co;2.

Milbrandt, J. A., and M. K. Yau, 2005: A multimoment bulk microphysics parameterization. Part I: Analysis of the role of the spectral shape parameter. *J. Atmos. Sci.*, **62**, 3051–3064, https://doi.org/10.1175/jas3534.1.

Mishchenko, M. I., L. D. Travis, and D. W. Mackowski, 1996: *T*-matrix computations of light scattering by nonspherical particles: A review. *Journal of Quantitative Spectroscopy and Radiative Transfer*, **55**, 535–575, https://doi.org/10.1016/0022-4073(96)00002-7.

Nešpor, V., W. F. Krajewski, and A. Kruger, 2000: Wind-induced error of raindrop size distribution measurement using a two-dimensional video disdrometer. *J. Atmos. Oceanic Technol.*, **17**, 1483–1492, https://doi.org/10.1175/1520-0426(2000)017<1483:Wieors>2.0.Co;2.

Porcù, F., L. P. D'Adderio, F. Prodi, and C. Caracciolo, 2014: Rain drop size distribution over the Tibetan Plateau. *Atmospheric Research*, **150**, 21–30, https://doi.org/10.1016/j.atmosres.2014.07.005.

Ryzhkov, A. V., S. E. Giangrande, and, T. J. Schuur, 2005: Rainfall Estimation with a Polarimetric Prototype of WSR-88D. *J. Appl. Meteorol.*, **44**, 502–515, https://doi.org/10.1175/jam2213.1.

Schönhuber, M., G. Lammer, and W. L. Randeu, 2007: One decade of imaging precipitation measurement by 2D-video-distrometer. *Advances in Geosciences*, **10**, 85–90, https://doi.org/10.5194/adgeo-10-85-2007.

Stout, G. E., and E. A. Mueller, 1968: Survey of relationships between rainfall rate and radar reflectivity in the measurement of precipitation. *J. Appl. Meteorol.*, **7**, 465–474, https://doi.org/10.1175/1520-0450(1968)007<0465:Sorbrr>2.0.Co;2.

Thurai, M., and V. N. Bringi, 2005: Drop axis ratios from a 2D

video disdrometer. *J. Atmos. Oceanic Technol.*, **22**, 966–978, https://doi.org/10.1175/jtech1767.1.

Thurai, M., C. R. Williams, and V. N. Bringi, 2014: Examining the correlations between drop size distribution parameters using data from two side-by-side 2D-video disdrometers. *Atmospheric Research*, **144**, 95–110, https://doi.org/10.1016/j.atmosres.2014.01.002.

Thurai, M., P. N. Gatlin, and V. N. Bringi, 2016: Separating stratiform and convective rain types based on the drop size distribution characteristics using 2D video disdrometer data. *Atmospheric Research*, **169**, 416–423, https://doi.org/10.1016/j.atmosres.2015.04.011.

Tokay, A., and D. A. Short, 1996: Evidence from tropical raindrop spectra of the origin of rain from stratiform versus convective clouds. *J. Appl. Meteorol.*, **35**, 355–371, https://doi.org/10.1175/1520-0450(1996)035<0355:Eftrso>2.0.Co;2.

Tokay, A., P. G. Bashor, E. Habib, and T. Kasparis, 2008: Raindrop size distribution measurements in tropical cyclones. *Mon. Wea. Rev.*, **136**, 1669–1685, https://doi.org/10.1175/2007mwr2122.1.

Tokay, A., W. A. Petersen, P. Gatlin, and M. Wingo, 2013: Comparison of raindrop size distribution measurements by collocated disdrometers. *J. Atmos. Oceanic Technol.*, **30**, 1672–1690, https://doi.org/10.1175/jtech-d-12-00163.1.

Ulbrich, C. W., 1983: Natural variations in the analytical form of the raindrop size distribution. *J. Climate Appl. Meteorol.*, **22**, 1764–1775, https://doi.org/10.1175/1520-0450(1983)022<1764:Nvitaf>2.0.Co;2.

Ulbrich, C. W., and D. Atlas, 2007: Microphysics of raindrop size spectra: Tropical continental and maritime storms. *J. Appl. Meteorol. Climatol.*, **46**, 1777–1791, https://doi.org/10.1175/2007jamc1649.1.

Wang, G. L., R. R. Zhou, S. L. Zhaxi, and S. N. Liu, 2021: Raindrop size distribution measurements on the Southeast Tibetan Plateau during the STEP project. *Atmospheric Research*, **249**, 105311, https://doi.org/10.1016/j.atmosres.2020.105311.

Wen, G., H. Xiao, H. L. Yang, Y. H. Bi, and W. J. Xu, 2017: Characteristics of summer and winter precipitation over northern China. *Atmospheric Research*, **197**, 390–406, https://doi.org/10.1016/j.atmosres.2017.07.023.

Wen, L., K. Zhao, G. F. Zhang, M. Xue, B. W. Zhou, S. Liu, and X. C. Chen, 2016: Statistical characteristics of raindrop size distributions observed in East China during the Asian summer monsoon season using 2-D video disdrometer and Micro Rain Radar data. *J. Geophys. Res.*, **121**, 2265–2282, https://doi.org/10.1002/2015jd024160.

Wen, L., K. Zhao, Z. L. Yang, H. N. Chen, H. Huang, G. Chen, and Z. W. Yang, 2020: Microphysics of stratiform and convective precipitation during meiyu season in eastern China. *J. Geophys. Res.*, **125**, e2020JD032677, https://doi.org/10.1029/2020jd032677.

Williams, C. R., A. B. White, K. S. Gage, and F. M. Ralph, 2007: Vertical structure of precipitation and related microphysics observed by NOAA profilers and TRMM during NAME 2004. *J. Climate*, **20**, 1693–1712, https://doi.org/10.1175/jcli4102.1.

Wu, Y. H., and L. P. Liu, 2017: Statistical characteristics of raindrop size distribution in the Tibetan Plateau and southern China. *Adv. Atmos. Sci.*, **34**, 727–736, https://doi.org/10.1007/s00376-016-5235-7.

Yuan, X., K. Yang, H. Lu, Y. Wang, and X. G. Ma, 2023: Impacts of moisture transport through and over the Yarlung Tsangpo Grand Canyon on precipitation in the eastern Tibetan Plateau. *Atmospheric Research*, **282**, 106533, https://doi.org/10.1016/j.atmosres.2022.106533.

Zhang, G., J. Vivekanandan, and E. Brandes, 2001: A method for estimating rain rate and drop size distribution from polarimetric radar measurements. *IEEE Trans. Geosci. Remote Sens.*, **39**, 830–841, https://doi.org/10.1109/36.917906.

Zhang, G. F., J. Vivekanandan, E. A. Brandes, R. Meneghini, and T. Kozu, 2003: The shape–slope relation in observed gamma raindrop size distributions: Statistical error or useful information?. *J. Atmos. Oceanic Technol.*, **20**, 1106–1119, https://doi.org/10.1175/1520-0426(2003)020<1106:Tsriog>2.0.Co;2.

Zhang, G. F., S. Luchs, A. Ryzhkov, M. Xue, L. Ryzhkova, and Q. Cao, 2011: Winter precipitation microphysics characterized by polarimetric radar and video disdrometer observations in central oklahoma. *J. Appl. Meteorol. Climatol.*, **50**, 1558–1570, https://doi.org/10.1175/2011jamc2343.1.

Zhu, L., C. S. Lu, X. Q. Xu, X. He, J. J. Li, S. Luo, Y. Wang, and F. Wang, 2024: The probability density function related to shallow cumulus entrainment rate and its influencing factors in a large-eddy simulation. *Adv. Atmos. Sci.*, **41**, 173–187, https://doi.org/10.1007/s00376-023-2357-6.